remote sensing

MDPI

Article

Retrieving Surface Deformation of Mining Areas Using ZY-3 Stereo Imagery and DSMs

Wenmin Hu [1], Jiaxing Xu [1,*], Wei Zhang [2], Jiatao Zhao [1,3] and Haokun Zhou [1,3]

[1] The National Joint Engineering Laboratory of Internet Applied Technology of Mines, China University of Mining and Technology, Xuzhou 221116, China; huwm@cumt.edu.cn (W.H.); ts20160197p31@cumt.edu.cn (J.Z.); ts20160202p31@cumt.edu.cn (H.Z.)
[2] State Key Laboratory of Coal Resources and Safe Mining, China University of Mining and Technology, Xuzhou 221116, China; zhangwei@cumt.edu.cn
[3] School of Environment and Spatial Informatics, China University of Mining and Technology, Xuzhou 221116, China
* Correspondence: xujx@cumt.edu.cn; Tel.: +86-0516-83590839

Abstract: Measuring surface deformation is crucial for a better understanding of spatial-temporal evolution and the mechanism of mining-induced deformation, thus effectively assessing the mining-related geohazards, such as landslides or damage to surface infrastructures. This study proposes a method of retrieving surface deformation by combining multi-temporal digital surface models (DSMs) with image homonymous features using China's ZY-3 satellite stereo imagery. DSM is generated from three-line-array images of ZY-3 satellite using a rational function model (RFM) as the imaging geometric model. Then, elevation changes in deformation are extracted using the difference of DSMs acquired at different times, while planar displacements of deformation are calculated using image homonymous features extracted from multi-temporal digital orthographic maps (DOMs). Scale invariant feature transform (SIFT) points and line band descriptor (LBD) lines are selected as two kinds of salient features for image homonymous features generation. Cross profiles are also extracted for deformation in typical regions. Four sets of stereo imagery acquired in 2012 to 2022 are used for deformation extraction and analysis in the Fushun coalfield of China, where surface deformation is quite distinct and coupled with rising and descending elevation together. The results show that 21.60% of the surface in the study area was deformed from 2012 to 2017, while a decline from 2017 to 2022 meant that 17.19% of the surface was deformed with a 95% confidence interval. Moreover, the ratio of descending area was reduced to 6.44% between 2017 and 2022, which is lower than the ratios in other years. The slip deformation area in the west open pit mine is about 1.22 km^2 and the displacement on the south slope is large, reaching an average of 26.89 m and sliding from south to north to the bottom of the pit between 2012 and 2017, but elevations are increased by an average of about 16.35 m, involving an area of about 0.86 km^2 between 2017 and 2022 due to the restoration of the open pit. The results demonstrate that more quantitative features and specific surface deformation can be retrieved in mining areas by combining image features with DSMs derived from ZY-3 satellite stereo imagery.

Keywords: surface deformation; ZY-3 stereo imagery; digital surface model (DSM); homonymous features; mining areas

check for updates

Citation: Hu, W.; Xu, J.; Zhang, W.; Zhao, J.; Zhou, H. Retrieving Surface Deformation of Mining Areas Using ZY-3 Stereo Imagery and DSMs. *Remote Sens.* **2023**, *15*, 4315. https://doi.org/10.3390/rs15174315

Academic Editors: Radosław Juszczak, Krzysztof Tajduś and Paweł Ocłoń

Received: 21 July 2023
Revised: 25 August 2023
Accepted: 30 August 2023
Published: 1 September 2023

Copyright: © 2023 by the authors. Licensee MDPI, Basel, Switzerland. This article is an open access article distributed under the terms and conditions of the Creative Commons Attribution (CC BY) license (https://creativecommons.org/licenses/by/4.0/).

1. Introduction

Surface deformation is very essential for the characterization and better understanding of many natural and anthropogenic processes [1–5]. Due to the influence of mining activities such as excavation, dumping, blasting, drainage, transportation and so forth, surface deformation is very distinct and complicated in mining areas, which leads to many geological disasters, such as landslide, subsidence, collapse, cracking and damage to the buildings or other facilities [5]. Therefore, retrieving accurate surface deformation is of great

significance for a better understanding of the spatial-temporal evolution and mechanism of mining-induced geohazards, and also for effectively assessing exploitation safety.

Traditional monitoring of surface deformation usually adopts the method with observations at some sparse points using GPS, or precise leveling, which can repeat the observations at these points and obtain high-precision displacements of surface. However, since the measurements only implement at a few points, it is not suitable for deformation monitoring in a large area for its low spatial resolution and efficiency, and requiring a lot of human and financial costs. With the application of remote sensing techniques, surface deformation monitoring using high-resolution satellite data has been widely used and it can well realize the monitoring over a very large area. Many related studies have been carried out on surface deformation such as deformation in volcanoes [1], glacier movement [6–10], landslides [4,11–13], permafrost [14], land subsidence [15,16], deformation in mining areas [5,17–20] or other geohazards detections [2,21–24]. A variety of approaches using interferometric synthetic aperture radar (InSAR) or space-borne differential InSAR have been used for the monitoring of mining-induced displacements in many mining areas [5]. However, rapid change or deformation with large amplitude in an abruptly morphing area could lead to a failure to estimate the correct displacement for temporal decorrelation and phase unwrapping of SAR images [16]. Moreover, limited by the side-looking observations of SAR images, the acquired deformation or displacement is always along the radar line of sight (LoS) direction, it is still difficult to retrieve the actual 3D deformation. Therefore, some improved methods have emerged such as integrating the heterogeneous observations to determine an optimal 3D movement of the glacier using variance component estimation (VCE) algorithms to weigh four kinds of observations in the adjustment solution [9], combining optical images with SAR or digital elevation model (DEM) for the automated detection of debris-covered glaciers using a random forest classifier [6], or fusing multi-source data for landslide displacement prediction [11].

As the basic topographic data, DSM depicts the elevations of the top surface above the bare earth. It is valuable to detect and compute the height of all overlying objects on the terrain such as buildings or other ground features. The height or elevation of DSM can be a complement to the traditional 2D spectral information offered by high resolution satellite imagery, and has been applied in terrain feature extraction, geomorphologic change, building mapping, or obtaining the spatial information of specific targets [25–27]. DSM or DEM derived from satellite photogrammetry can provide visible features and 3D information of the surface in a large area, and has become a very important means for Earth observation [28]. Compared with two-dimensional change detection using optical images, DSM subtraction is a traditional method for three-dimensional change detection, which can provide the surface relief change for land use [29–31]. Moreover, periodic satellite imagery with high resolution can provide convenient data sources for multi-temporal DSMs and DOMs extraction, and thus can be a support for the monitoring of surface deformation or change, environmental planning and governance in the mining areas [3,5,32]. However, DSM for 3D observations and changes usually focus on the change in elevation direction and rarely on specific changes in the 2D plane, while satellite photogrammetry also provides 2D images, that means the planar displacements can also be retrieved from measurable 2D images, such as DOMs. Different from the VCE method to determine the weights of multiple observations from different platforms to reconstruct the velocity of 3D movement [9], using DSM derived from satellite photogrammetry can combine the height information of DSM with the corresponding 2D planar observations directly from the same observation platform, where inconsistencies from observation errors between different platforms can be reduced or not considered.

ZY-3 satellite is the first civilian high-resolution stereo mapping optical satellite in China, which was launched in January 2012 and has been operated in orbit for more than 10 years [33]. The satellite was equipped with panchromatic three-line-array cameras, the forward (FWD) and backward (BWD) cameras are installed at inclinations of $\pm 22^{\circ}$ from the nadir (NAD) camera with a base-to-height ratio of 0.87. The spatial resolution is 3.5 m

for FWD and BWD cameras, and 2.1 m for the NAD camera. The satellite images are widely used for the mapping and production of 1:50,000 scale cartographic products, and many experiments demonstrate that the planar and vertical accuracy of DSM and orthomap derived from ZY-3 satellite stereo imagery is better than 3 and 2 m, respectively [33–39]. Therefore, multi-temporal DSMs generated by ZY-3 satellite imagery can be used as important data sources for surface deformation or landform changes. However, the mining areas are often intervened by natural terrain and artificial terrain, and the abrupt and gradient terrains coexist. Surface deformation in mining areas is frequent and relatively complicated due to the mining disturbances. Large and frequent deformation in mining areas could affect the stability of ground control points (GCPs), which would further affect the accuracies of DSMs and change detection.

To reveal the capabilities of ZY-3 satellite stereo imagery for surface deformation in mining areas, especially with acute surface changes, this study proposes a method of retrieving surface deformation by combining multi-temporal DSMs with image homonymous features in mining areas. DSMs are derived from ZY-3 satellite stereo imagery with the sensor model expressed by rational polynomial coefficients (RPC), which are refined using high-accuracy GCPs and tie points in the block adjustment with an affine transformation model. The homonymous features are generated from matched SIFT points or LBD lines of multi-temporal orthographic images, and then are used to obtain the horizontal displacements of surface. The difference of DSMs reflects the deformation of surface in elevation direction, while the displacement of homonymous features reflects the variation of surface deformation in the plane direction. The rest of this study is organized as follows: Section 2 presents information on the study area and data used in the processing. Section 3 is the methodology of retrieving surface deformation using DSMs and homonymous features of DOMs derived from ZY-3 satellite stereo images. The results of surface deformation characteristics for the mining surface are described in Section 4. The discussion and conclusions are listed in Sections 5 and 6, respectively.

2. Study Area and Data

2.1. Study Area

The study area is located in the Fushun coalfield in Fushun city, Liaoning Province, Northeast China. Fushun was once the largest fuel production base in China and was known as "coal city". The Hunhe river runs from east to west, with a high terrain in the east and low in the west. It belongs to the alluvial plain area of the Hunhe river, with an average elevation of about 65~99 m [40]. As shown in Figure 1, Fushun coalfield is located in the south of the Hunhe river, and there are two open pit mines in the region, the west open pit mine and the east open pit mine, which are located in the west and east of the Fushun coalfield, respectively. The principal coal beds of Fushun coalfield are low-sulfur subbituminous and bituminous in rank, and they are of limnic origin and contained in the 55 m thick Eocene Guchengzi Formation [41]. The surface deformation in the study area is quite distinct and is coupled with rising and descending elevation together, because the mining exploitation, waste dumping and artificial backfilling for restoration exist simultaneously.

The west open pit has been mined for more than a hundred years since 1901. It is the largest open-pit coal mine in Asia, with a length of 6.6 km from east to west, a width of 2.2 km from north to south and a total area of about 13.2 square kilometers. In its hundred years of mining history, it mainly adopted horizontal stratification mining, with a vertical depth of nearly 400 m, and the main products are coal and oil shale. However, surface deformation, including landslides, subsidence, surface collapse and fracture, has occurred since the 1990s due to the long mining activities and inadequate treatment of coal mine waste rocks. Since August 2010, in addition to the mining area, ground cracks began to appear in the southern slope of the west open pit. Surface deformation, especially in the north and south slopes, is gradually becoming more serious [42]. The cracks extended, widened and deepened continuously, and developed from the initial point shape to the

linear shape rapidly. Serious displacement and deformation led to the uplift of the bottom, the landslides of slopes, as well as to damage to the surrounding environment. From 2009 to 2015, the mining of the west open pit began to adopt small zoning mining, and the mining range ensured that the slope angle of the north side was not greater than 30° [42]. By 2017, mining activities had almost ceased due to the need for environmental protection. In June 2019, the coal mining of the west open pit was officially closed, from mining to ecological restoration [40,41]. The east open pit is smaller than the west open pit, with a length of about 5.7 km from east to west, a width of about 1.9 km from north to south and a total area of about 9.2 square kilometers. After 2001, the mining of the oil shale of coal seam top was recovered. The two mining pits are typical negative landforms formed by artificial open-pit mining in the region. At the same time, there are also three typical positive landforms formed by mining dump sites in the study area, which are the east dump site, west dump site and Wangliang dump site, whose elevation at the highest point is over 200 m.

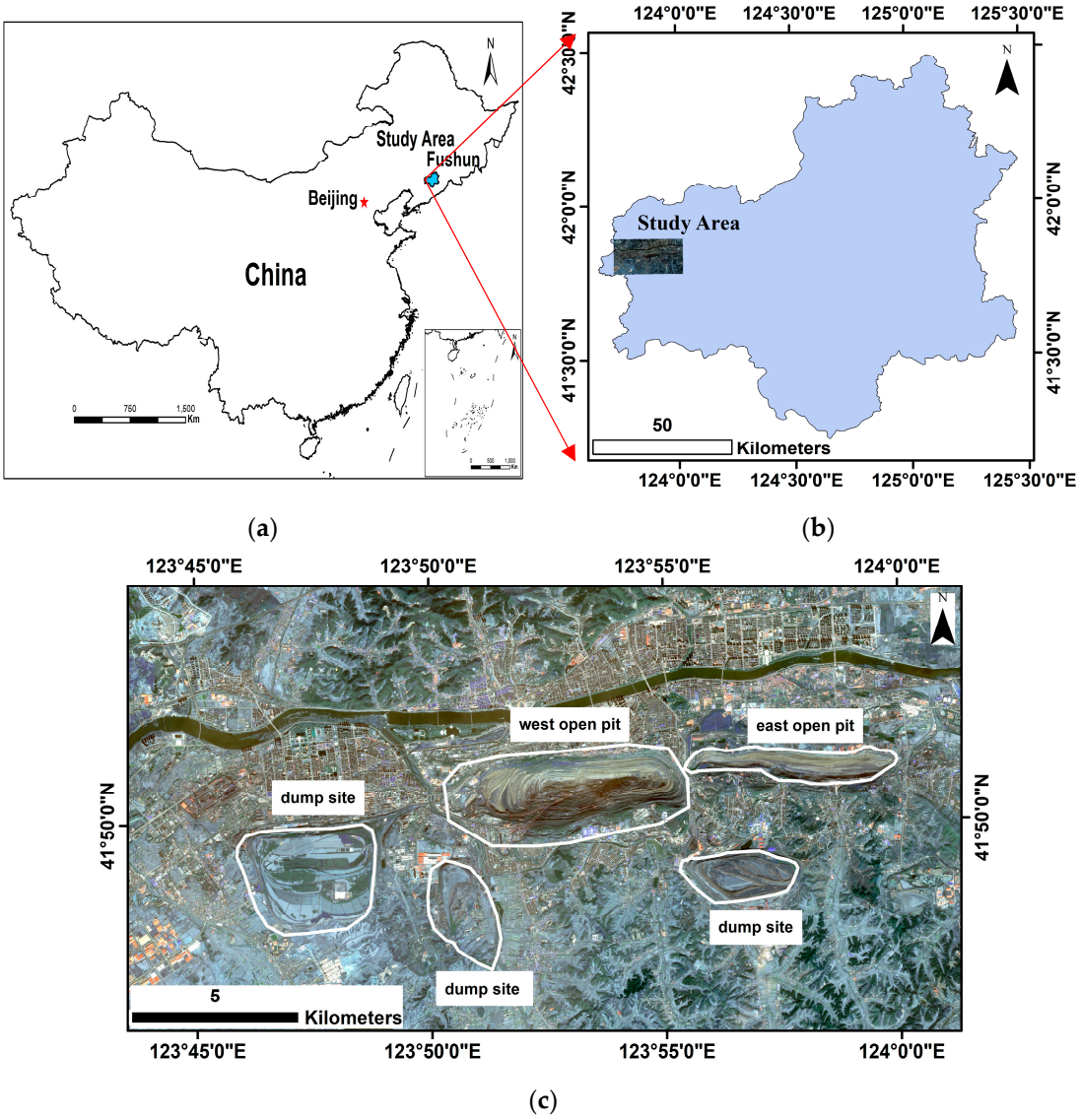


Figure 1. *Cont.*



(**d**)

Figure 1. The location and typical surface maps of study area. (**a**) Location of Fushun city in China. (**b**) Location of study area in Fushun city. The rectangle marks the coverage of the study area in this study. (**c**) Locations of five typical regions in the study area. The white polygons indicate the boundaries of the typical regions, which are the main open mining areas and dump sites in the study area. The base image is the multispectral image captured by China's ZY-3 satellite in October in 2015. (**d**) A site map of west open pit mine. Photo taken in July 2014.

2.2. Data

Four factors, including the complete coverage of the image of the study area, the cloud cover being less than 10% and not distributing directly above the study area, there being no snow cover and the closing time of the west open pit mine, are considered comprehensively to select the stereo images of ZY-3 satellite. As listed in Table 1, in order to test the effect of surface deformation detection in mining areas, four sets of ZY-3 stereo images acquired in May of 2012, October of 2015, June of 2017 and March of 2022 are selected to generate the corresponding DSM and retrieve the surface deformation in the mining areas, respectively. The images from 2012 are the first suitable stereo images of ZY-3 satellite in the study area, while images acquired in 2015, 2017 and 2022 correspond to the stage of small zoning mining, the stage of mining cessation, and the stage of closure and restoration in the west open pit, respectively. The satellite operates in a sun-synchronous orbit with an orbital altitude about 505.98 km, whose semi-major axis is about 6876.98 km. The orbital inclination is about 97.42° and the orbit recursive period is about 59 days [34].The FWD and BWD cameras are installed at inclinations of ±22° from the NAD camera with a base-to-height ratio of 0.87. The spatial resolution is 3.5 m for FWD and BWD cameras, and 2.1 m for the NAD camera. The ground sample distance (GSD) of DSMs derived from stereo imagery is 10 m in this study. The study area is located in the overlapping coverage area of the four stereo images with different acquisition times, which is represented by the green rectangle in Figure 2a.

Table 1. Datasets of ZY-3 stereo imagery used in this study.

Acquisition Time	Center Point (°)	Stereo Imagery	GSD of DSM (m)
23 May 2012	E124.105, N41.749	NAD+BWD	10
24 October 2015	E124.010, N41.987	NAD+BWD+FWD	10
5 June 2017	E123.823, N41.986	NAD+BWD+FWD	10
30 March 2022	E123.863, N41.757	NAD+BWD+FWD	10

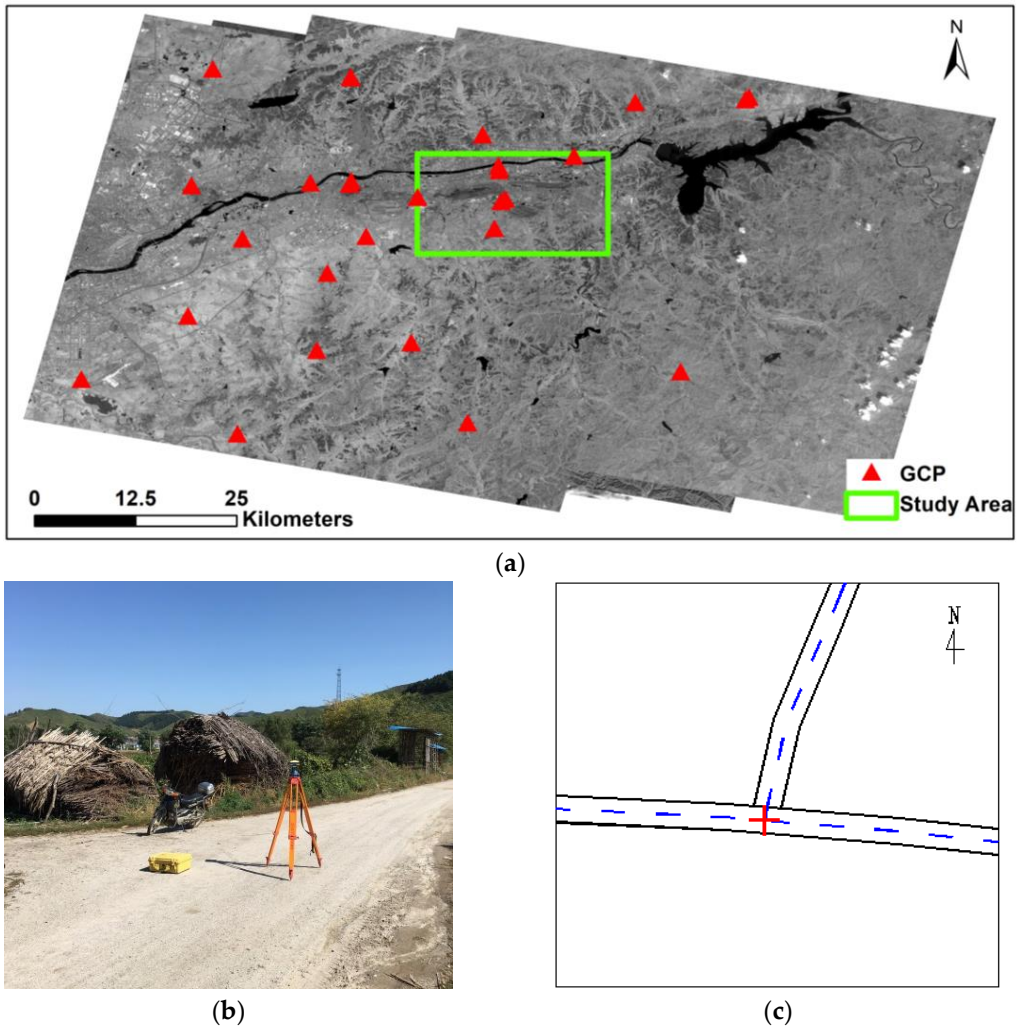


Figure 2. GCPs used in this study. (**a**) Distribution of GCPs on ZY-3 stereo images. The green rectangle represents the overlapping areas of the four sets of stereo images in the study area. The red triangles represent the locations of GCPs. (**b**) GCP measured though RTK in the center point of road intersections. (**c**) Locations of prick points for GCPs.

A total of thirty-four GCPs are used to refine the RPC coefficients of ZY-3 stereo images in the block adjustment, which can improve the accuracy of derived DSM. The accuracy of elevation measurement is within 0.01 m and the accuracy of prick points reaches sub-pixel level in image space. The distribution of GCPs on ZY-3 stereo images is displayed in Figure 2a. All the points are obtained though RTK in May 2016 and July 2017, which are generally located in stable, open and flat areas without topographic changes, such as road corner points or the center point of road intersections, as shown in Figure 2b,c.

3. Methodology

Surface deformation is retrieved from the difference of DSMs and the displacements of image homonymous features after co-registration. The difference of DSMs reflects the change of surface elevation in the region, while the displacements of homonymous features reflect the variation of surface deformation in the plane direction. The process of retrieving surface deformation by combining DSMs with the image homonymous features in the mining areas is shown in Figure 3.

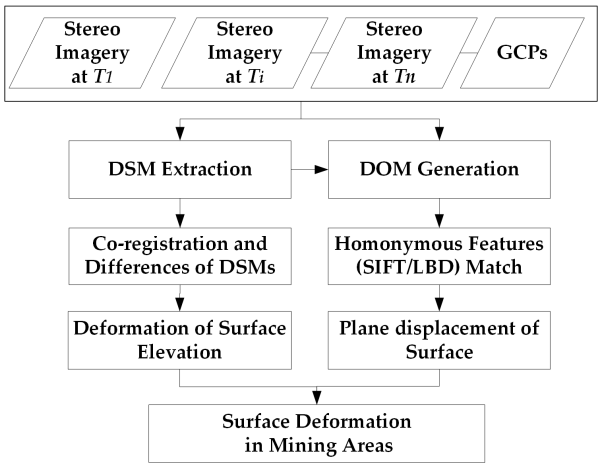


Figure 3. The process of retrieving surface deformation by combining DSMs with image homonymous features using ZY-3 stereo imagery.

3.1. DSM and DOM Generation

DSM is generated from the three line-array images of ZY-3 satellite using RFM as the imaging geometric model, which is an accurate fitting of the rigorous geometric imaging model. According to the RPC in the RFM, the relationship between the 2D image coordinates and 3D ground coordinates is defined as follows:

$$l = \frac{P_1(lon, lat, H)}{P_2(lon, lat, H)}, s = \frac{P_3(lon, lat, H)}{P_4(lon, lat, H)} \tag{1}$$

where (l, s) are the image coordinates and (lon, lat, H) are their corresponding normalized ground geodetic coordinates and P_1, P_2, P_3, P_4 are the RPC of the RFM, which is built on the WGS84 geocentric coordinate system.

Figure 4 shows the process of RPC refinement and DSM generation using refined RPC in the block adjustment. An affine transformation of the image refinement model is adopted to refine the RPC in the block adjustment with high-accuracy GCPs, using the method described in a previous study to improve the quality and evaluate the accuracies of DSM derived from ZY-3 stereo imagery [43]. The affine model is defined as follows:

$$\begin{cases} \Delta l = a_0 + a_1 \cdot s + a_2 \cdot l \\ \Delta s = b_0 + b_1 \cdot s + b_2 \cdot l \end{cases} \tag{2}$$

where (l, s) and $(\Delta l, \Delta s)$ are the observations and corrections of image coordinates, respectively. $(a_0, a_1, a_2, b_0, b_1, b_2)$ are the coefficients of the affine model. Then, the error equation can be constructed as follows:

$$\begin{cases} F_l = \frac{P_1(lon,lat,h)}{P_2(lon,lat,h)} - l - \Delta l \\ F_S = \frac{P_3(lon,lat,h)}{P_4(lon,lat,h)} - s - \Delta s \end{cases} \tag{3}$$

According to this model, the error equation point by point and normal equations of block adjustment can be established with the affine coefficients of the RFM and the corresponding ground coordinates of each dense tie point as unknowns. The least square method is adopted to iteratively solve these unknowns. Then, DSM is derived with refined RPC and refined dense points with a spatial resolution of 10 m for all ZY-3 DSM in this study.

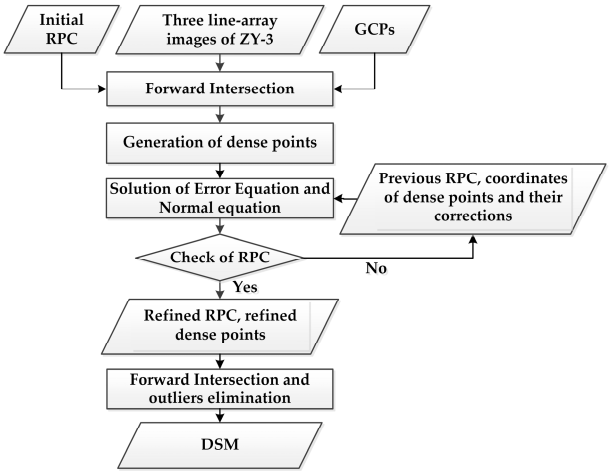


Figure 4. DSM generation using refined RPC in the block adjustment.

DOMs are the images with orthophoto properties, which can avoid the image distortion caused by optical system, scanning nonlinearity, attitudes state or surface topography. All nadir images are ortho-rectified to DOMs in a unified coordinate system using the GCPs and the corresponding DSM [44]. Then, the DOMs acquired at different times can be used as the data source for extraction and matching of image homonymous features, which can be the indicators of planar displacements for surface deformation.

3.2. Elevation Changes from Difference of DSMs

The difference in sequential DSMs is used to quantify the elevation change for surface deformation [30]. It is calculated as follow:

$$\Delta H_{ij} = H_{ij}(t_2) - H_{ij}(t_1) \tag{4}$$

where t_1 and t_2 are the imaging times of different DSMs and $H_{ij}(t_1)$, $H_{ij}(t_2)$ are the values of elevation at the grid location (i, j) of DSM on time t_1 and t_2, respectively. ΔH_{ij} is the difference of elevation at (i, j) from t_1 to t_2.

Considering the error from DSM and elevation subtraction operation, the change of surface elevation needs significance detection to determine the actual change area. Here, a method of t-test in statistics is used to convert the elevation change into the corresponding t statistic as follows [45]:

$$t = \frac{|H(t_2) - H(t_1)|}{\sigma_{\Delta H}} \tag{5}$$

where $|H(t_2) - H(t_1)|$ is the absolute difference of two DSMs in elevation direction and $\delta_{\Delta H}$ is the RMSE of elevation difference between the two DSMs. According to the law of error propagation, $\delta_{\Delta H}$ can be calculated as follows:

$$\sigma_{\Delta H} = \sqrt{\sigma^2_{H(t_1)} + \sigma^2_{H(t_2)}} \tag{6}$$

where $\sigma_{H(t_1)}$ and $\sigma_{H(t_2)}$ are the values of elevation RMSE of the two DSMs. According to the principle of the t-test, the threshold of surface elevation change is segmented as follows:

$$\frac{|H(t_2) - H(t_1)|}{\sigma_{\Delta H}} > T \tag{7}$$

where T is a given threshold for surface elevation change, and $\sigma_{\Delta H}$ can be used as the critical value for the detectable minimum deformation with the given confidence level. When the difference of elevation meets the threshold in Formula (7), it can be considered that the surface elevation in the region has changed. At the same time, the positive and

negative values of the difference are used to distinguish the rise and fall of elevation, respectively. Generally, 68% (confidence level α = 0.32) and 95% (confidence level α = 0.05) are used in the *t*-test as the significance test thresholds, and the corresponding thresholds are 1 and 1.96, respectively. Two kinds of results of surface elevation change are extracted under these two confidence levels, respectively.

3.3. Surface Planar Displacements from Image Homonymous Features

As feature-based matching methods are often more efficient and can better handle geometrical deformation [46], image homonymous features are used as the indicators to measure the planar geometric deformation in this study. Image homonymous features are the same features or structure extracted from two or more images acquired at different times. Since the DOMs are all unified in the same coordinate system, the displacements between homonymous point pairs and line pairs can represent the planar displacements of surface deformation.

As shown in Figure 5, the left and the right rectangles represent two nadir DOMs acquired at different times, $P1$ and $P2$ represent one pair of the homonymous feature points, $L1$ and $L2$ represent the matched homonymous feature lines, respectively. Assuming the coordinates of $P1$ and $P2$ on the two nadir DOMs are (x_1, y_1) and (x_2, y_2), respectively, then the displacement between the homonymous point pairs in the east–west direction is $x_2 - x_1$, the displacement in the north–south direction is $y_2 - y_1$ and the linear displacement distance D_P between this homonymous points pair is as follows:

$$D_P = \sqrt{(x_1 - x_2)^2 + (y_1 - y_2)^2} \tag{8}$$

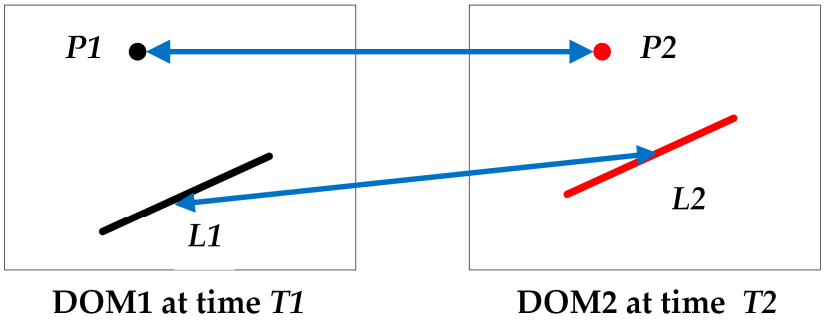


Figure 5. Displacements calculated from image homonymous features.

Similarly, assuming that $L1$ and $L2$ represent the matched homonymous feature lines and (x_{L1}, y_{L1}) and (x_{L2}, y_{L2}) are the midpoint coordinates of $L1$ and $L2$, respectively, then the displacements D_L between the homonymous line pairs can be described by the distance between the midpoints of $L1$ and $L2$ as follows:

$$D_L = \sqrt{(x_{L1} - x_{L2})^2 + (y_{L1} - y_{L2})^2} \tag{9}$$

Moreover, the offset angle between the homonymous lines is

$$\Delta\theta = \theta_2 - \theta_1 \tag{10}$$

where θ_1 and θ_2 are the inclinations of homonymous lines on two nadir DOMs with different acquisition times.

Since the most popular features are the points, such as keypoints or interest points, the SIFT points are selected as one kind of salient homonymous features. SIFT extracts keys point as the local extrema in a difference of Gaussians (DoG) pyramid, filtered using the Hessian matrix of the local intensity values, thus achieving scale and rotation invariance, which has been a very classic and popular feature description algorithm that can be used

to perform reliable matching between different views [47]. However, due to the large amplitude of surface deformation inside the open-pit caused by mining, it is difficult to match suitable feature points between images acquired at different times. For this reason, a line feature described by LBD is also adopted to extract homonymous line features. The LBD algorithm combines the local appearance of line segment and geometric constraints, which can extract and match effective line targets in complex environments [48,49]. The specific extraction and matching algorithm refer to the corresponding literatures, and are not described here. Therefore, the homonymous points or lines pairs are derived from the SIFT points and LBD lines after matching, thus they are used for the calculation of surface planar displacements.

4. Results

4.1. DSM and Surface Elevation Changes

Four DSMs derived from ZY-3 stereo imagery, acquired in 2012, 2015, 2017 and 2022, are used to calculate the difference of DSMs, and thus evaluate the elevation changes for surface using the method in Section 3.2. Figure 6 shows the DSMs derived from ZY-3 stereo imagery acquired in 2012, 2015, 2017 and 2022, respectively. All DSMs are generated using a grid with a spatial resolution of 10 m here. As the DSMs are all generated with refined RPC using the method displayed in Figure 4, the specific statistics and elevation accuracy of DSMs are listed in Table 2. The root mean square error (RMSE) of DSM elevations acquired in 2012, 2015, 2017 and 2022 is 3.07 m, 1.72 m, 2.07 m and 2.37 m, respectively. The average accuracy of elevation according to the values of RMSE is 2.31 m for these DSMs in this region, which is consistent with the previous research results [38,43,50,51].

Figure 7 shows the spatial distribution of elevation differences between DSMs acquired in different years. It is clear that surface deformation in and around the open pit, especially the west open pit, is very dramatic. In addition, elevations of the surface in the area of dump sites also changes significantly. Table 3 lists the statistics of elevation differences between these DSMs and the results of elevation changes according to 68% (confidence level $\alpha = 0.32$) and 95% (confidence level $\alpha = 0.05$) as the significance test thresholds for surface elevation deformation. Table 4 lists the detailed distribution of elevation changes for surface deformation. According to the ratio and ranges of elevation changes, elevation increase and decrease are mixed together. From 2012 to 2017, 42.86% of surface in this area is deformed with 68% confidence interval, while 21.60% is deformed with a 95% confidence interval. From 2017 to 2022, 38.86% of surface is deformed with 68% confidence interval, while 17.19% is deformed with a 95% confidence interval. Moreover, the ratio of descending area to the whole study area is 15.31% (68% confidence interval) and 6.44% (95% confidence interval) between 2017 and 2022, which is lower than the ratios in other years. From the results, the overall ratio of surface deformation detected by the elevation of DSMs shows a decreasing trend as the years progressed.

Significant deformed areas are analyzed through extracting the regions with elevations changed and measuring the properties of regions. Using a 95% confidence interval (1.96 times $\sigma_{\Delta H}$), districts with obvious elevation changes and an area of deformation over 0.07 km^2 are extracted. The results are superimposed on the multispectral image in Figure 8a,b, showing the distribution of significant deformed areas in the two periods, 2012 to 2017, and 2017 to 2022, respectively. Yellow and red polygons draw the boundaries of the districts where the elevations descend and rise significantly, respectively. Deformation in the west open pit, the east open pit and the two dump sites are all obvious but their changes in the two periods, from 2012 to 2017 and 2017 to 2022, are not the same.

In the west open pit, it is mainly manifested as the elevation descending on the north slope and the south slope, which is caused by the slip of the north and south slopes between 2012 and 2017. As shown in Figure 8a, the yellow polygons in the west open pit show the slip regions, where the observed elevation is reduced by an average of 23.19 m, the area of the deformation is about 1.22 km^2 and the ground volume change is about 3.15×10^7 m^3. At the same time, the elevation also presents an uneven rise in the east–west direction in the

open pit during this period, involving an area of about 5.18 km^2 where elevation increases by an average of 34.95 m and there is a volume change of nearly 1.88 $\times$ 10^8 m^3. However, the change between 2017 and 2022 in the west open pit is significantly different from the change between 2012 and 2017 due to the official closure and the restoration of the open pit. Elevations are increased by an average of about 16.35 m on the north slope and the south slope, involving an area of about 0.86 km^2 and volume change of about 1.21 $\times$ 10^7 m^3. Elevations in the middle of open pit show an increase of about 11.19 m on average because of the project of pit backfilling, mainly involving an area of about 2.14 km^2 and volume change of about 2.43 $\times$ 10^8 m^3.

In the east open pit, surface deformation is mainly dominated by a reduction in elevation as the open pit was still in the process of mining between 2012 and 2017. The average descending elevation is about 22.87 m, covering an area of about 4.66 km^2 and volume change of nearly 1.07 $\times$ 10^8 m^3. With the reduction in mining and the restoration of the open pit, the average elevation of the pit has increased by 12.88 m on average, covering an area of about 2.49 km^2, and volume change of about 3.20 $\times$ 10^7 m^3, from 2017 to 2022.

Table 2. Statistics of elevations of DSMs derived from ZY-3 stereo imagery (unit: meter).

Acquisition Time	Minimum of Elevation	Maximum of Elevation	Average of Elevation	Accuracy of Elevation
23 May 2012	−325.84	247.99	104.31	3.07
24 October 2015	−324.37	276.31	106.11	1.72
5 June 2017	−325.89	328.74	105.13	2.07
30 March 2022	−160.73	236.05	107.71	2.37

Table 3. Statistics of differences of DSMs and actual surface deformation in elevation detected using threshold between DSMs acquired in different years.

Compared Years	Minimum (m)	Maximum (m)	Average (m)	Standard Deviation (m)	Change Ratio (68%)	Change Ratio (95%)	RMSE of Elevation Differences $\sigma_{\Delta H}$
2012–2015	−220.55	489.70	1.65	11.95	49.55%	24.98%	3.52
2015–2017	−502.31	596.94	−0.93	11.43	46.12%	22.54%	2.69
2012–2017	−211.03	537.12	0.81	12.39	42.86%	21.60%	3.70
2017–2022	−293.75	342.63	1.10	8.55	38.86%	17.19%	3.14

Table 4. Ratios of surface elevation changes detected using ZY-3 DSMs.

Compared Years	Range of Elevation Changes	Ratio	Range of Elevation Changes	Ratio
2012–2015	$<-1.96\delta_{\Delta H}$	8.81%	$>1.96\delta_{\Delta H}$	16.17%
	$-1.96\delta_{\Delta H}$~$-\delta_{\Delta H}$	9.75%	$\delta_{\Delta H}$~$1.96\delta_{\Delta H}$	14.82%
	Total descending (68%)	18.56%	Total rising (68%)	30.99%
2015–2017	$<-1.96\delta_{\Delta H}$	15.05%	$>1.96\delta_{\Delta H}$	8.08%
	$-1.96\delta_{\Delta H}$~$-\delta_{\Delta H}$	13.50%	$\delta_{\Delta H}$~$1.96\delta_{\Delta H}$	9.48%
	Total descending (68%)	28.55%	Total rising (68%)	17.57%
2012–2017	$<-1.96\delta_{\Delta H}$	9.54%	$>1.96\delta_{\Delta H}$	12.06%
	$-1.96\delta_{\Delta H}$~$-\delta_{\Delta H}$	9.40%	$\delta_{\Delta H}$~$1.96\delta_{\Delta H}$	11.86%
	Total descending (68%)	18.94%	Total rising (68%)	23.92%
2017–2022	$<-1.96\delta_{\Delta H}$	6.44%	$>1.96\delta_{\Delta H}$	10.75%
	$-1.96\delta_{\Delta H}$~$-\delta_{\Delta H}$	8.87%	$\delta_{\Delta H}$~$1.96\delta_{\Delta H}$	12.80%
	Total descending (68%)	15.31%	Total rising (68%)	23.55%

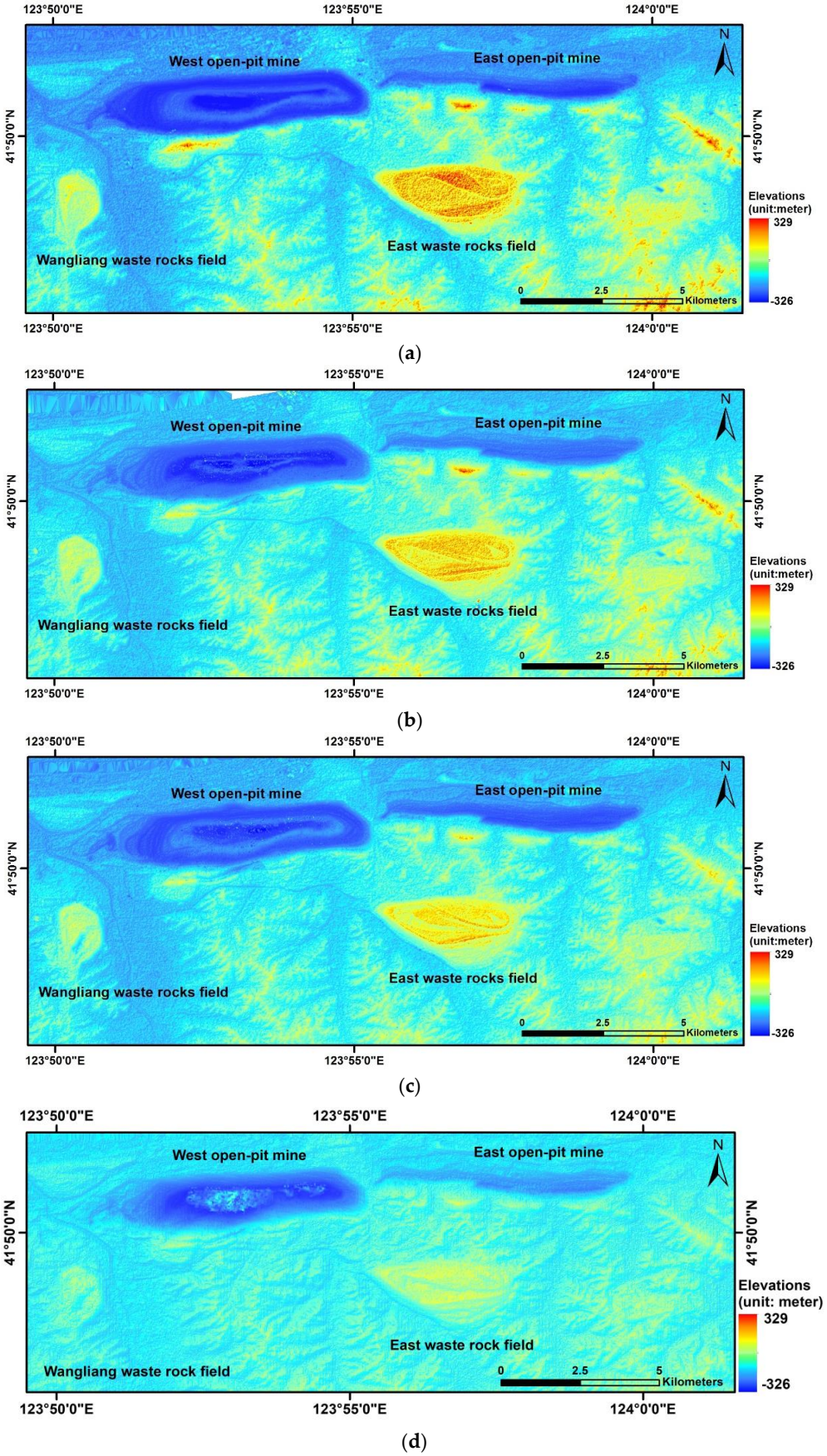


Figure 6. DSMs derived from ZY-3 stereo imagery acquired in (**a**) 2012, (**b**) 2015, (**c**) 2017 and (**d**) 2022.

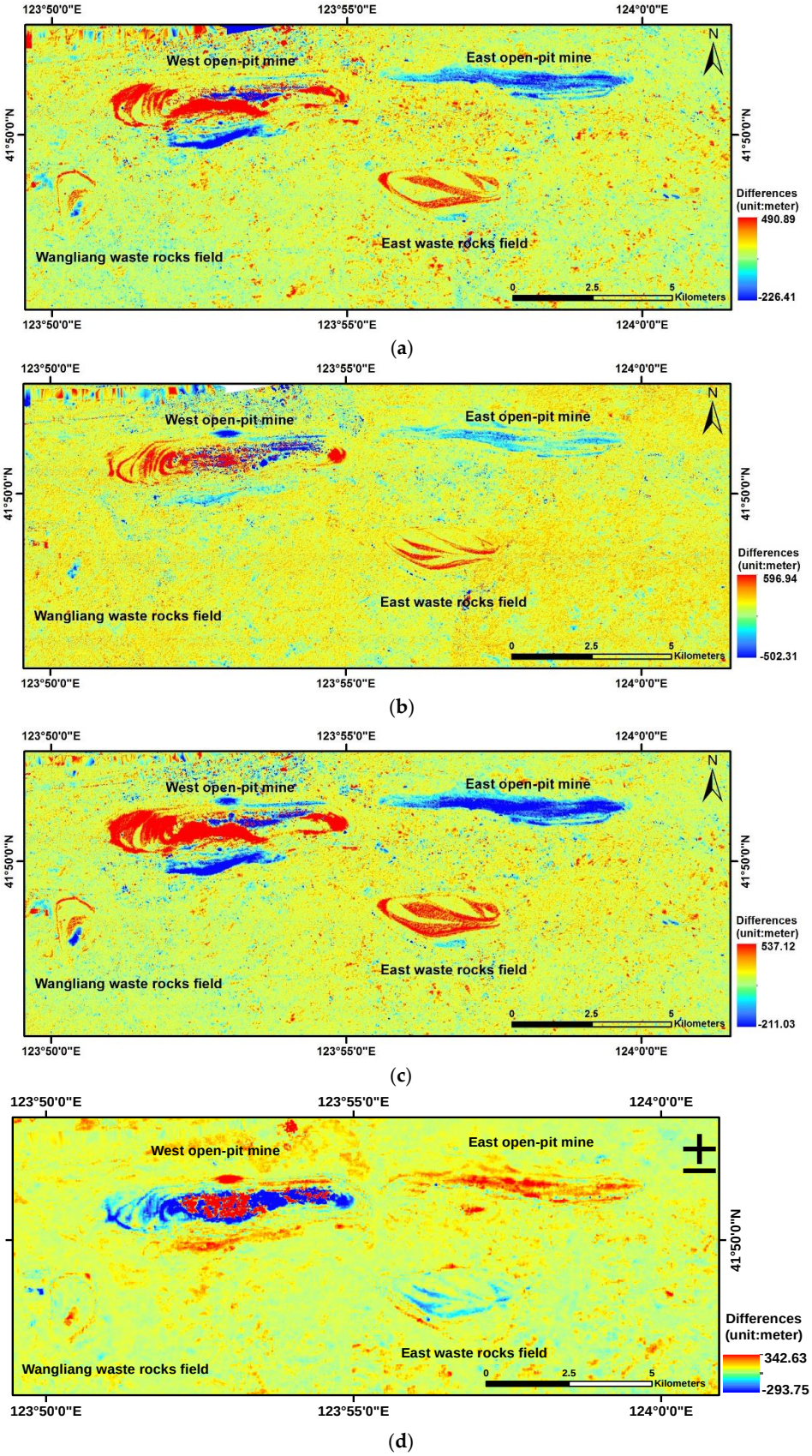


Figure 7. Surface elevation changes from difference of DSMs. (**a**) Difference between DSM of 2012 and DSM of 2015. (**b**) Difference between DSM of 2015 and DSM of 2017. (**c**) Difference between DSM of 2012 and DSM of 2017. (**d**) Difference between DSM of 2017 and DSM of 2022.

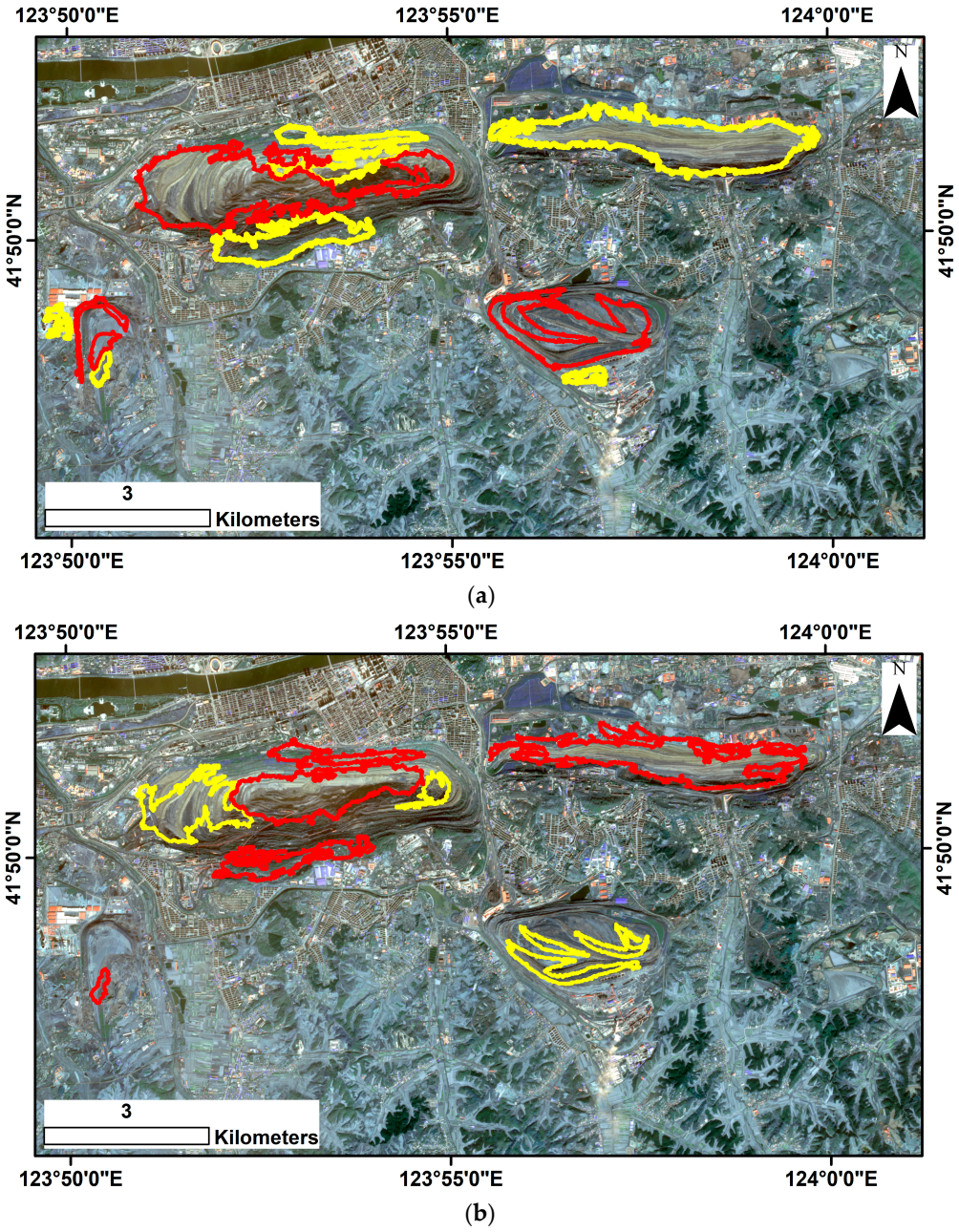


Figure 8. Districts of surface deformation with significant elevation changes (**a**) between 2012 and 2017, and (**b**) between 2017 and 2022. Red polygons represent the districts of surface deformation with obvious rising elevations and yellow polygons represent the districts of surface deformation with obvious descending elevations.

In addition, elevations in the east waste rocks field and Wangliang waste rocks field mainly increase between 2012 and 2017. The average elevation is increased by about 11.86~17.84 m, covering a total area of about 3.11 km^2 and volume change of about 5.38 $\times$ 10^7 m^3. At the same time, there are also three regions with obvious elevation descending, mainly located in the edge of the dump sites, covering a total area of about 0.43 km^2 and volume change of about 7.21 $\times$ 10^6 m^3. The reduced range of average elevations here is between 12.10 and 24.50 m. Between 2017 and 2022, the surface in the Wangliang waste rocks field is partially uplifted by an average of 15.55 m, with an area of about 0.10 km^2 and volume change of nearly 1.52 $\times$ 10^6 m^3. On the other hand, elevations of the east waste rocks field are mainly reduced by about 13.34 m, covering about 0.85 km^2 and with a volume change of about 1.14 $\times$ 10^7 m^3.

4.2. Planar Displacement from Image Homonymous Features

SIFT and LBD algorithms are used here to extract the homonymous points and lines, respectively. Taking DOM images from 2012 to 2017 as an example, in the west open pit and its surrounding areas, displacements calculated from the homonymous points extracted by SIFT matching are about 0.02 m in the east–west direction and about 1.38 m in the north–south direction, respectively. Figure 9 shows the distribution of SIFT points in and around the pit in 2012, 2015 and 2017, respectively. SIFT points are barely matched inside the pit or the slope regions due to the severe deformation.

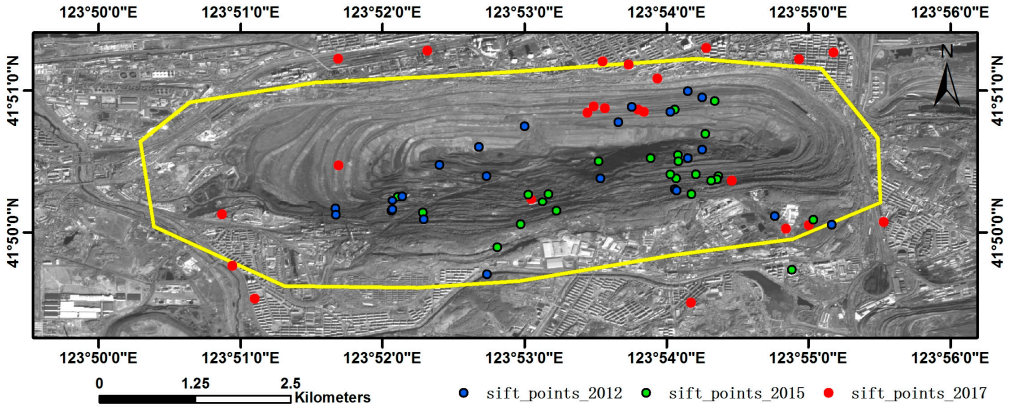


Figure 9. Distribution of SIFT points features in the west open pit. Blue, green and red dots represent the SIFT points features extracted from DOM of 2012, 2015 and 2017, respectively.

In order to further acquire the deformation details in the pit, the homonymous lines detected by LBD are shown in Figure 10. Although the line features are not evenly distributed and few in number, some valid homonymous line pairs are still detected in the pit and on the south slope. According to the calculation, the displacement shown by the lines outside but still near the pit (red ellipse) is about 1.69 m with an average offset angle 0.56° pointing north in the pit, while the displacement inside the pit or around the south slope is larger, reaching an average of 26.89 m and sliding from south to north to the bottom of the pit.

4.3. Surface Deformation from Profiles

From west to east, six lines in Figure 11a indicate the detailed locations of the chosen profiles that crossed the west open pit. Yellow polygons represent the districts of surface deformation with obvious descending elevations detected in Figure 8 between 2012 and 2017. Elevation values along the profile are extracted from ZY-3 DSM in 2012, 2017 and 2012. The results of elevation variation along the profiles are shown in Figure 11b–g, respectively.

It can be seen from the profile results that elevation rise and fall coexist in this pit. Profile 1 in the westernmost and Profile 6 in the farthest east show that both elevations of 2017 and 2022 are higher than that of 2012 as a whole because the pit is in the backfilling stage without active mining in the eastern and western ends. Between 2012 and 2017, only a small part of the central region is being mined, which is why the bottom of the pit displayed by Profiles 2~5 appears undulating. At the same time, deformation caused by landslides on the north and south slope is very obvious. There is a large area of slip on the south slope, and the maximum drop is about 58.30 m (Profiles 3). A landslide on the north slope with a maximum drop of 45.32 m (Profiles 4) is smaller in scale than that on the south slope and occurred in a local region, so it is very obvious from the image.

However, Profiles 3~6 show that the bottom of the open pit is lifting from 2017 to 2022, because mining in the west open pit was officially stopped and it is undergoing restoration and post-mining treatment in this period. Furthermore, elevations in the southern part of all five Profiles 2~6 in 2022 are all higher than that in 2017, which means that the landslide (yellow polygon) has been contained.

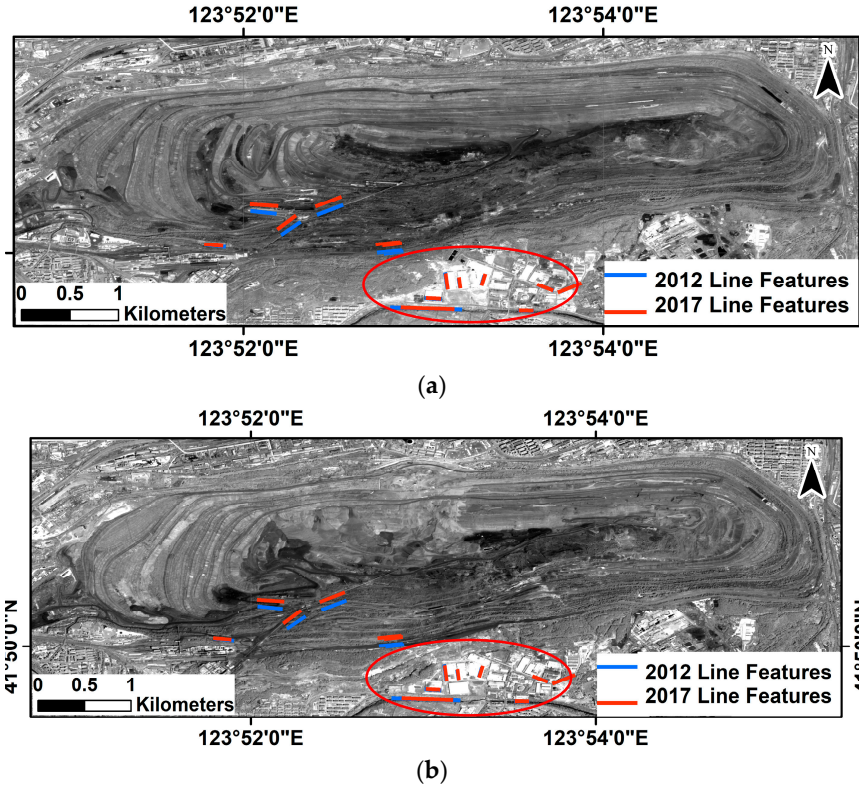


Figure 10. Planar displacement from homonymous LBD features. (**a**) LBD features overlaid on Nadir DOM of 2012. (**b**) LBD features overlaid on Nadir DOM of 2017. Blue and red lines represent the LBD features extracted from DOM of 2012 and 2017, respectively.

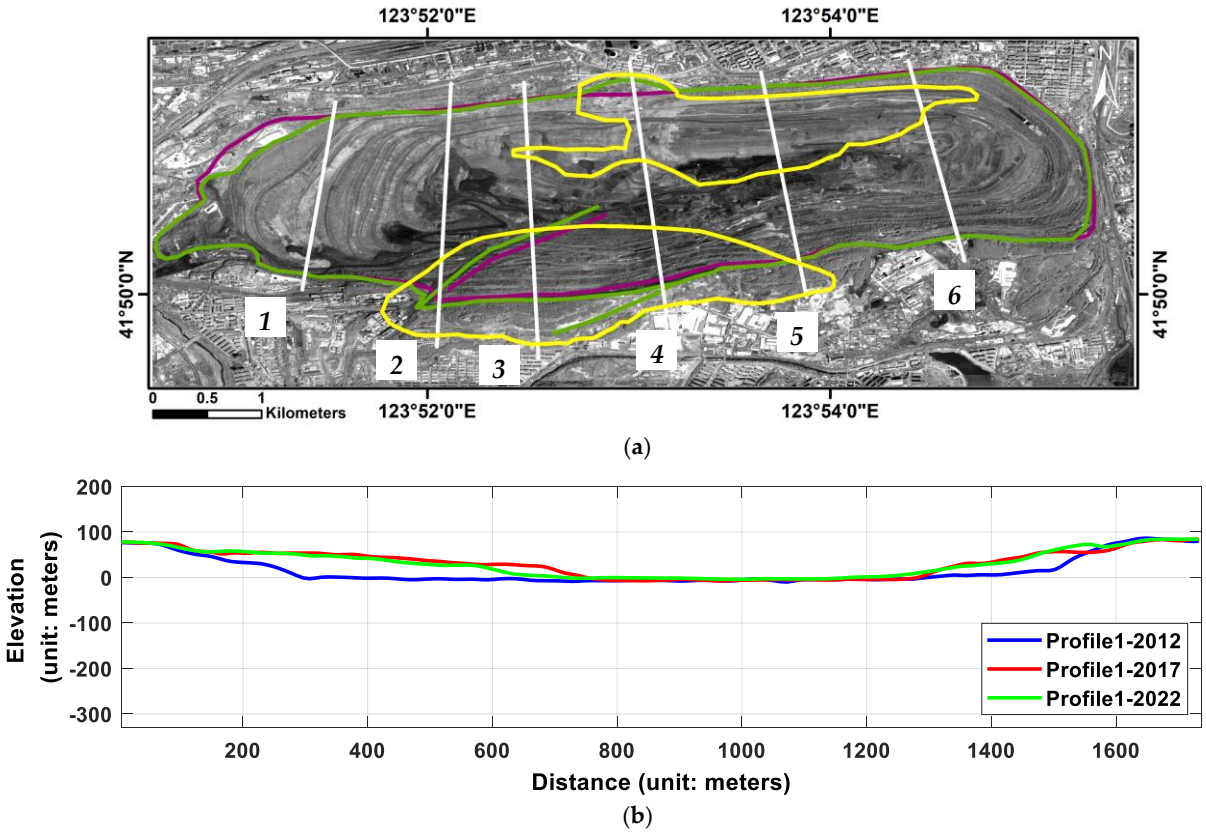
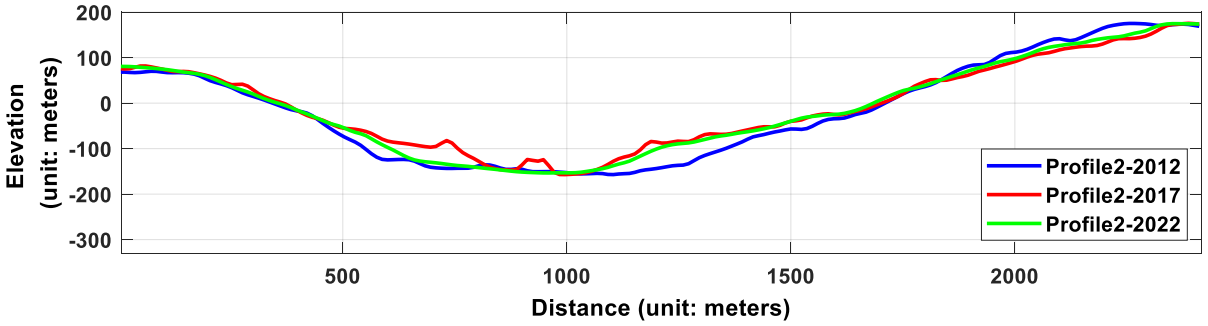
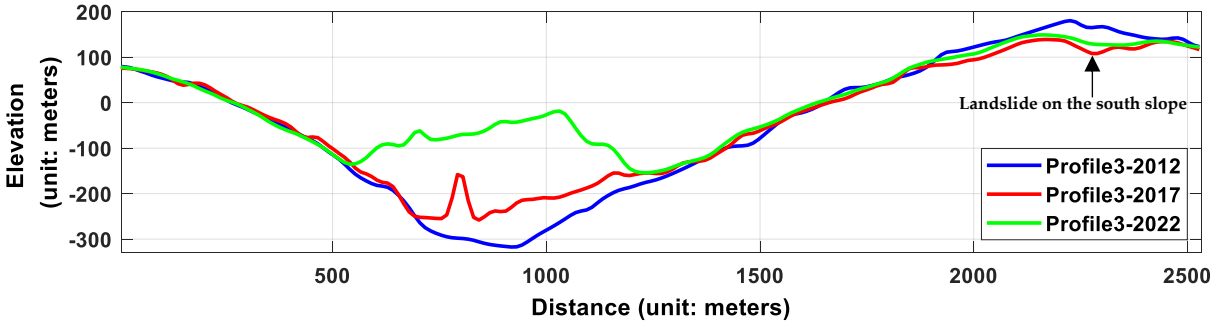


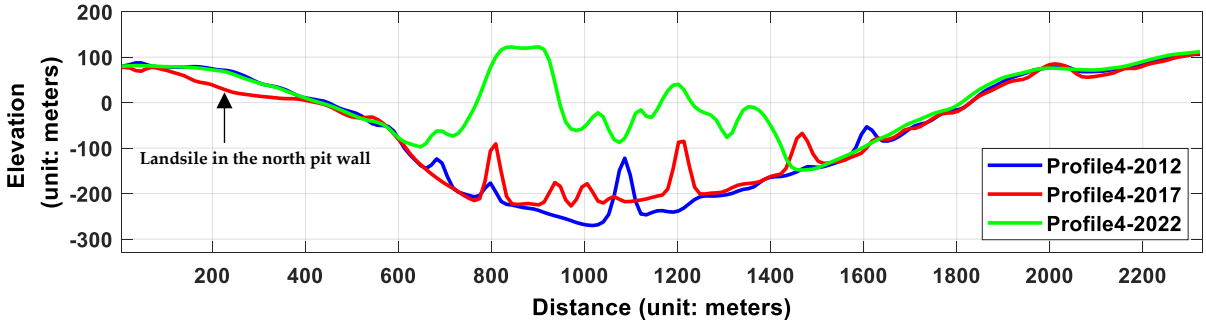
Figure 11. *Cont.*



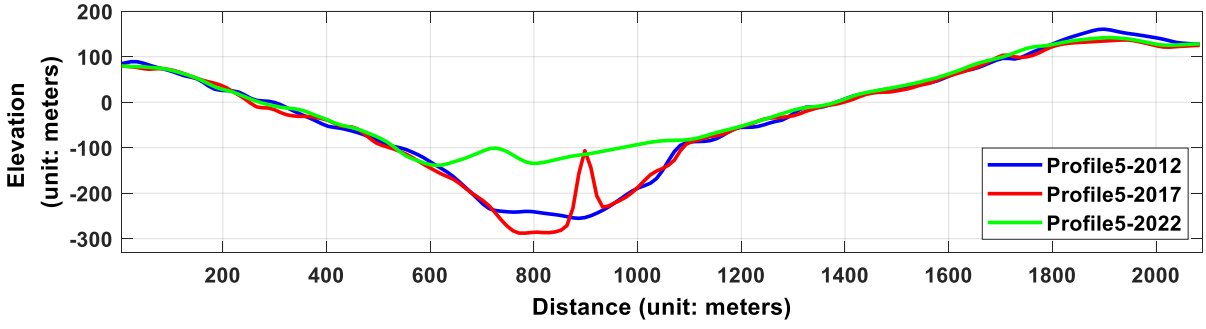
(**c**)



(**d**)



(**e**)



(**f**)

Figure 11. *Cont.*

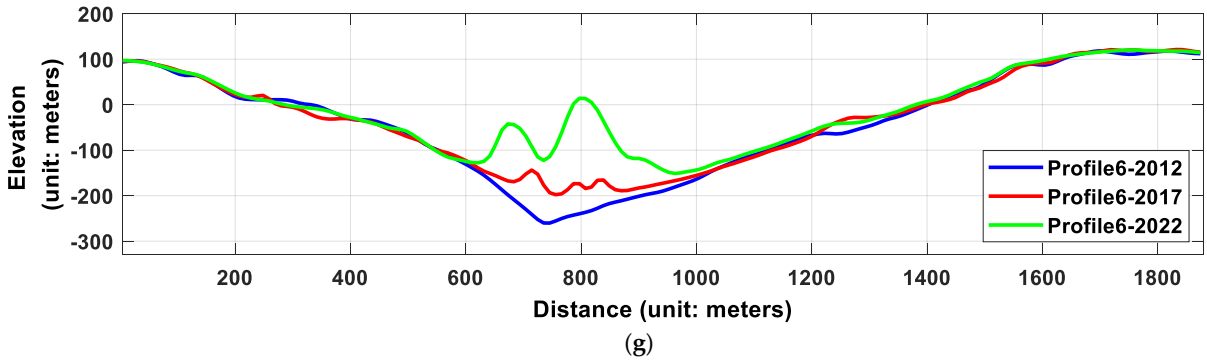


Figure 11. Surface deformation retrieved from profiles. (**a**) Distribution of profiles in west open pit. White lines represent the profiles in this region, purple and green polylines represent the edges of pit and the belt transport line in the pit in 2012 and 2017, respectively. Yellow polygons represent the districts of surface deformation with obvious descending elevations detected in Figure 8 between 2012 and 2017. (**b**–**g**) Surface deformation from Profiles 1~6 which are plotted in (**a**), respectively. Blue, red and green profiles represent the surface elevation along the profile in 2012, 2017 and 2022, respectively.

5. Discussion

5.1. Uncertainties of Extracted Deformation

It is evident that the results of surface deformation heavily depend on the strategy and data accuracy. The results support that the strategy of extracting the elevation deformation using the difference between DSMs acquired at different times, extracting planar displacements from image homonymous features and extracting cross profiles for deformation in typical regions in this study can obtain more comprehensive and specific deformation in the mining areas. In addition to deformation detection, more quantitative deformation is obtained, such as the amplitude, displacement, area and volume of the deformation.

However, the accuracy of DSMs and imagery may influence the accuracy of extracted parameters for deformation and then suppress the inadequacy of surface deformation analysis. ZY-3 imagery and its derived DSM are adopted to detect and extract the parameters for the elevation, planar displacement, area and volume of surface deformation. The elevation accuracy of DSMs is shown in Table 2, with an average value of about 2.31 m, and the average RMSE of elevation differences for extracted surface deformation is about 3.26 m from Table 4. According to the law of error propagation, the accuracy (RMSE) of retrieved deformation area and volume can be calculated as follows:

$$\sigma_S = \sqrt{\left(\frac{\partial S}{\partial W}\right)^2 \cdot \sigma_W^2 + \left(\frac{\partial S}{\partial L}\right)^2 \cdot \sigma_L^2}, \ \sigma_V = \sqrt{\left(\frac{\partial S}{\partial W}\right)^2 \cdot \sigma_W^2 + \left(\frac{\partial S}{\partial L}\right)^2 \cdot \sigma_L^2 + \left(\frac{\partial V}{\partial H}\right)^2 \cdot \sigma_H^2} \quad (11)$$

where L and W are the length and width of the grid. The size of DSM grid pixel is 10 m in this study and resolution of DOM is 2.1 m, which is the same as that of the nadir image. As the deformation areas are extracted pixel by pixel, and an accuracy of 0.5 pixels has been ensured in the DSM, the extracted parameters for deformation areas have an accuracy of $\sqrt{2}$ times the above accuracy. Table 5 lists the accuracies of extracted parameters for surface deformation in this study. The accuracies of extracted parameters not only depend on the accuracies of the basic measurements of deformation, but they are also related to the dimensional scales, such as spatial resolution and grid size of the data set.

On the other hand, the selection of image homonymous features will also affect the extraction of surface planar displacements. The homonymous SIFT points or LBD lines generated by feature-based matching method have translation, scale and rotation invariance, which means that these features are only valid for the deformation such as translational, rotation or scaling. It is difficult to match the appropriate homonymous features if the surface has a very complex deformation, such as distortion, disappearance or strong undulating changes. However, surface deformation in mining areas is often

complicated and with many forms of deformation that coexist in the disturbance of mining activities. Therefore, more invariant features or parameters can be considered for measuring more detailed surface deformation.

Table 5. Accuracies (RMSE) of extracted parameters for deformation.

Extracted Parameters	Symbol	RMSE
Elevation changes	$\overline{\sigma}_{\Delta H}$ *	3.26 m
Planar displacement	σ_D	2.84 m
Deformation area	σ_S	0.00071 km^2
Deformation volume	$\overline{\sigma}_V$ *	40.72 m^3

* Refers to the average accuracy for corresponding parameters.

5.2. Long-Term Monitoring of Deformation in Mining Areas

Four sets of stereo images of ZY-3 satellite, acquired in 2012 to 2022, are used for deformation detection and analysis in the Fushun coalfield. Surface deformation in mining areas is quite distinct and is coupled together with rising or declining elevation since the mining exploitation, waste dumping and artificial backfilling for restoration exist simultaneously. In the west open pit, the elevation-rising area is enlarging quickly for the artificial backfill process, especially between 2017 and 2022. The elevation-descending area is increasing and the amplitude gets larger over time between 2012 and 2017 for the large deformation of slope sliding. The deformation detected along the profiles also shows similar results in the pit. By 2022, the elevation-descending area caused by landslides has been suppressed, and the elevation on the north and south slopes has been raised, which shows the effect of backfill restoration. Since the launch of ZY-3 satellite in 2012, a large number of images of the Earth's surface have been obtained. With the passage of time and accumulation of imagery, more stereoscopic imagery can be adopted for surface monitoring, and long-term sequences can be obtained, which is of great significance for the spatial-temporal evolution of terrain and environmental changes in mining areas.

Compared with traditional monitoring with discrete point observations, the method from satellite observations is regional and the results and accuracy are distributed more evenly and naturally in space. At the same time, the method of DSM elevation change, combined with geometric deformation retrieved from image homonymous features, extracts the 3D deformation directly in the elevation, planar and profile directions, which is very helpful for the detailed quantification and analysis of surface deformation over a wide area. The deformation from differences of DSMs is regionally distributed and represents the overall change of elevations within the region. The profile deformation comes directly from the differences of DSMs, but it has a better performance for the vertical trend and distribution of deformation in typical regions. However, in contrast to the complete distribution of deformation in the elevation direction, surface planar deformation is also discrete with the points or lines features, and is not guaranteed to be detected in all areas because of the limited number of homonymous features in the area with severe deformation. In this study, two kinds of features, SIFT points and LBD lines, are used to analyze the planar displacements, but they can only work well in the local area of the south slope; no suitable homonymous features could be detected in the wider region. The fusion of deformations from more homonymous features or regional face invariant features, and the weight relationship between the features, should be considered for more detailed and complete 3D surface deformation.

6. Conclusions

This study proposes a method for retrieving surface deformation by combining multi-temporal DSMs with image homonymous features using China's ZY-3 satellite stereo imagery. It demonstrates the application and potential of ZY-3 satellite stereo imagery for mapping and quantifying the surface deformation in mining areas with a higher temporal frequency, especially in open-pit areas with large ground deformation. Four sets of stereo

imagery acquired in 2012 to 2022 are used for deformation extraction and analysis in the Fushun coalfield of China. In addition to deformation detection, the results show that more quantitative and specific surface deformation, such as the amplitude, displacement, area and volume of the deformation, can also be retrieved in mining areas. The following conclusions are obtained.

(1) The surface deformation in Fushun coalfield is quite distinct and is coupled together with elevation rising and descending, since mining exploitation, waste dumping and artificial backfilling for restoration exist simultaneously. A total of 21.60% of the surface in the study area is deformed from 2012 to 2017, while 17.19% of surface is deformed from 2017 to 2022 with a 95% confidence interval. The slip deformation regions are suppressed in the west open pit as the elevations are increased by an average of about 16.35 m, involving an area of about 0.86 km^2, between 2017 and 2022.

(2) The method of combining multi-temporal DSMs with image homonymous features can obtain more quantitative and specific surface deformation in mining areas. In addition to deformation detection, quantitative and detailed parameters of the deformation in the elevation, planar and profile directions can be obtained, which is of significance for surface deformation monitoring and environmental governance.

(3) Surface deformation, especially distinct deformation, such as large fractures or landslides, can be monitored in the long term using Chinese ZY-3 stereo imagery. However, the accuracy of extracted parameters of surface deformation are related to the accuracy of DSMs and the resolution of the imagery. It is necessary to consider using higher precision data to retrieve the deformation in some areas if the amplitude of the deformation is subtle or is less than the accuracy of data.

Author Contributions: Conceptualization, W.H. and J.X.; methodology, W.H. and J.Z.; software, W.H., H.Z. and J.Z.; validation, H.Z., J.Z. and W.Z.; formal analysis, W.H.; investigation, W.H.; resources, W.H. and J.X.; data curation, W.H., H.Z. and J.Z.; writing—original draft preparation, W.H.; writing—review and editing, W.H., J.X. and W.Z.; visualization, W.H.; supervision, J.X.; project administration, J.X. All authors have read and agreed to the published version of the manuscript.

Funding: This research was supported by the National Natural Science Foundation of China (grant no. 52374141).

Data Availability Statement: ZY-3 imagery can be inquired through the website, Natural Resource Satellite Remote Sensing Cloud Service Platform (http://sasclouds.com/english/home, accessed on 20 July 2023). Illustrations in this paper were subject to no copyright restrictions.

Acknowledgments: We are thankful for the editorial help as well as academic suggestions from the anonymous reviewers.

Conflicts of Interest: The authors declare no conflict of interest.

References

1. Camacho, A.G.; Fernández, J.; Samsonov, S.V.; Tiampo, K.F.; Palano, M. 3D multi-source model of elastic volcanic ground deformation. *Earth Planet. Sci. Lett.* **2020**, *547*, 116445. [CrossRef]
2. Huang, Q.; Wang, Y.; Xu, J.; Nishyirimbere, A.; Li, Z. Geo-hazard detection and monitoring using SAR and optical images in a snow-covered area: The Menyuan (China) test site. *ISPRS Int. J. Geo-Inf.* **2017**, *6*, 293. [CrossRef]
3. Qin, R.; Tian, J.; Reinartz, P. 3D change detection—Approaches and applications. *ISPRS-J. Photogramm. Remote Sens.* **2016**, *122*, 41–56. [CrossRef]
4. Samsonov, S.; Dille, A.; Dewitte, O.; Kervyn, F.; d'Oreye, N. Satellite interferometry for mapping surface deformation time series in one, two and three dimensions: A new method illustrated on a slow-moving landslide. *Eng. Geol.* **2020**, *266*, 105471. [CrossRef]
5. Yang, Z.F.; Li, Z.W.; Zhu, J.J.; Wang, Y.D.; Wu, L.X. Use of SAR/InSAR in mining deformation monitoring, parameter inversion, and forward predictions: A review. *IEEE Geosci. Remote Sens. Mag.* **2020**, *8*, 71–90. [CrossRef]
6. Lu, Y.; Zhang, Z.; Kong, Y.; Hu, K. Integration of optical, SAR and DEM data for automated detection of debris-covered glaciers over the western Nyainqentanglha using a random forest classifier. *Cold Reg. Sci. Technol.* **2022**, *193*, 103421. [CrossRef]
7. Bhambri, R.; Schmidt, S.; Chand, P.; Nüsser, M.; Haritashya, U.; Sain, K.; Tiwari, S.K.; Yadav, J.S. Heterogeneity in glacier thinning and slowdown of ice movement in the Garhwal Himalaya, India. *Sci. Total Environ.* **2023**, *875*, 162625. [CrossRef]
8. Singh, A.K.; Kumar, D.; Kumar, V.; Singh, D.S. Study of temporal response (1976–2019) and associated mass movement event (during 2017) of Meru glacier, Bhagirathi valley, Garhwal Himalaya, India. *Quat. Int.* **2020**, *565*, 12–21. [CrossRef]

9. Hu, J.; Li, Z.W.; Li, J.; Zhang, L.; Ding, X.L.; Zhu, J.J.; Sun, Q. 3-D movement mapping of the alpine glacier in Qinghai-Tibetan Plateau by integrating D-InSAR, MAI and Offset-Tracking: Case study of the Dongkemadi Glacier. *Glob. Planet. Change* **2014**, *118*, 62–68. [CrossRef]
10. Frey, H.; Paul, F. On the suitability of the SRTM DEM and ASTER GDEM for the compilation of topographic parameters in glacier inventories. *Int. J. Appl. Earth Obs. Geoinf.* **2012**, *18*, 480–490. [CrossRef]
11. Liu, Y.; Xu, C.; Huang, B.; Ren, X.; Liu, C.; Hu, B.; Chen, Z. Landslide displacement prediction based on multi-source data fusion and sensitivity states. *Eng. Geol.* **2020**, *271*, 105608. [CrossRef]
12. Wolter, A.; Roques, C.; Gröble, J.; Ivy-Ochs, S.; Christl, M.; Loew, S. Integrated multi-temporal analysis of the displacement behaviour and morphology of a deep-seated compound landslide (Cerentino, Switzerland). *Eng. Geol.* **2020**, *270*, 105577. [CrossRef]
13. Xie, S.; Liang, Y.; Zheng, Z.; Liu, H. Combined forecasting method of landslide deformation based on MEEMD, approximate entropy, and WLS-SVM. *ISPRS Int. J. Geo-Inf.* **2017**, *6*, 5. [CrossRef]
14. Han, J.; Lu, P. Retrieving surface deformation of the Qinghai-Tibet railway across permafrost areas from InSAR. In Proceedings of the IGARSS 2020—2020 IEEE International Geoscience and Remote Sensing Symposium, Waikoloa, HI, USA, 26 September–2 October 2020; pp. 3074–3077.
15. Tang, W.; Zhao, X.; Motagh, M.; Bi, G.; Li, J.; Chen, M.; Chen, H.; Liao, M. Land subsidence and rebound in the Taiyuan basin, northern China, in the context of inter-basin water transfer and groundwater management. *Remote Sens. Environ.* **2022**, *269*, 112792. [CrossRef]
16. Ren, C.J.; Chen, H.X.; Bai, C.W.; Yan, L.L. Surface deformation detection method in mining subsidence based on GCP quadratic surface correction model in InSAR. In Proceedings of the 2022 IEEE International Geoscience and Remote Sensing Symposium (IGARSS 2022), Kuala Lumpur, Malaysia, 17–22 July 2022; pp. 2554–2557.
17. Hu, W.M.; Wu, L.X.; Zhang, W.; Liu, B.; Xu, J.X. Ground deformation detection using China's ZY-3 stereo imagery in an opencast mining area. *ISPRS Int. J. Geo-Inf.* **2017**, *6*, 361. [CrossRef]
18. Zhao, J.; Konietzky, H. Numerical analysis and prediction of ground surface movement induced by coal mining and subsequent groundwater flooding. *Int. J. Coal Geol.* **2020**, *229*, 103565. [CrossRef]
19. Shi, S.; Guo, Z.; Ding, P.; Tao, Y.; Mao, H.; Jiao, Z. Failure mechanism and stability control technology of slope during open-pit combing underground extraction: A case study from Shanxi province of China. *Sustainability* **2022**, *14*, 8939. [CrossRef]
20. Zhao, B.C.; Yu, X.Y.; Wang, J.D. Study on surface movement and deformation by mining in loess gully region. In Proceedings of the International Conference on Sustainable Energy and Environmental Engineering (ICSEEE 2012), Guangzhou, China, 29–30 December 2012; pp. 3005–3009.
21. Tang, C.; Tanyas, H.; van Westen, C.J.; Tang, C.; Fan, X.; Jetten, V.G. Analysing post-earthquake mass movement volume dynamics with multi-source DEMs. *Eng. Geol.* **2019**, *248*, 89–101. [CrossRef]
22. Liu, K.; Ding, H.; Tang, G.; Song, C.; Liu, Y.; Jiang, L.; Zhao, B.; Gao, Y.; Ma, R. Large-scale mapping of gully-affected areas: An approach integrating Google Earth images and terrain skeleton information. *Geomorphology* **2018**, *314*, 13–26. [CrossRef]
23. Wang, R.; Zhang, S.; Pu, L.; Yang, J.; Yang, C.; Chen, J.; Guan, C.; Wang, Q.; Chen, D.; Fu, B.; et al. Gully erosion mapping and monitoring at multiple scales based on multi-source remote sensing data of the Sancha river catchment, Northeast China. *ISPRS Int. J. Geo-Inf.* **2016**, *5*, 200. [CrossRef]
24. Cimoli, E.; Marcer, M.; Vandecrux, B.; Bøggild, C.E.; Williams, G.; Simonsen, S.B. Application of low-cost UASs and digital photogrammetry for high-resolution snow depth mapping in the Arctic. *Remote Sens.* **2017**, *9*, 1144. [CrossRef]
25. Nemmaoui, A.; Aguilar, F.J.; Aguilar, M.A.; Qin, R. DSM and DTM generation from VHR satellite stereo imagery over plastic covered greenhouse areas. *Comput. Electron. Agric.* **2019**, *164*, 104903. [CrossRef]
26. Xiao, W.; Cao, H.; Tang, M.; Zhang, Z.; Chen, N. 3D urban object change detection from aerial and terrestrial point clouds: A review. *Int. J. Appl. Earth Obs. Geoinf.* **2023**, *118*, 103258. [CrossRef]
27. Yousif, A.M.; Dimitri, B.; Fanar, M.A.; Petra, H. DTM Extraction and building detection in DSMs having large holes. In Proceedings of the Conference on Remote Sensing Technologies and Applications in Urban Environments VI, Online, 13–17 September 2021; p. 118640H.
28. Li, D.R.; Wang, M. A review of high resolution optical satellite surveying and mapping technology. *Spacecr. Recovery Remote Sens.* **2020**, *41*, 1–11.
29. Wei, H.; Li, S.; Li, C.; Zhao, F.; Xiong, L.; Tang, G. Quantification of Loess Landforms from Three-Dimensional Landscape Pattern Perspective by Using DEMs. *ISPRS Int. J. Geo-Inf.* **2021**, *10*, 693. [CrossRef]
30. James, L.A.; Hodgson, M.E.; Ghoshal, S.; Latiolais, M.M. Geomorphic change detection using historic maps and DEM differencing: The temporal dimension of geospatial analysis. *Geomorphology* **2012**, *137*, 181–198. [CrossRef]
31. Yue, Z.; Hu, W.; Liu, B.; Liu, Y.; Sun, X.; Zhao, Q.; Di, K. Quantitative analysis of the morphology of martian gullies and insights into their formation. *Icarus* **2014**, *243*, 208–221. [CrossRef]
32. Lv, G.; Xiong, L.; Chen, M.; Tang, G.; Sheng, Y.; Liu, X.; Song, Z.; Lu, Y.; Yu, Z.; Zhang, K.; et al. Chinese progress in geomorphometry. *J. Geogr. Sci.* **2017**, *27*, 1389–1412. [CrossRef]
33. Tang, X.M.; Wang, H.Y.; Zhou, P.; Ouyang, S.D.; Yue, Q.X. Data and product system of ZY-3 satellite. *Satell. Appl.* **2020**, *25*, 14–18.
34. Li, D.R. China's first civilian three-line-array stereo mapping satellite: ZY-3. *Acta Geod. Cartogr. Sin.* **2012**, *41*, 317–322.
35. Cao, H.Y.; Dai, J.; Xu, C.; Liu, F. China's ZY-3 satellite and its application. *Satell. Appl.* **2020**, *10*, 11–13.

36. Wang, M.; Yang, B.; Li, D.; Gong, J.; Pi, Y. Technologies and applications of block adjustment without control for ZY-3 images covering China. *Geomat. Inf. Sci. Wuhan Univ.* **2017**, *42*, 427–433.
37. Yang, B.; Wang, M.; Xu, W.; Li, D.; Gong, J.; Pi, Y. Large-scale block adjustment without use of ground control points based on the compensation of geometric calibration for ZY-3 images. *ISPRS-J. Photogramm. Remote Sens.* **2017**, *134*, 1–14. [CrossRef]
38. Zhang, G.; Jiang, Y.H.; Li, D.R.; Huang, W.C.; Pan, H.B.; Tang, X.M.; Zhu, X. In-orbit geometric calibration and validation of ZY-3 linear array sensors. *Photogramm. Rec.* **2014**, *29*, 68–88. [CrossRef]
39. Zhu, X.; Tang, X.; Zhang, G.; Liu, B.; Hu, W.; Pan, H. Long-periodic analysis of boresight misalignment of Ziyuan3-01 three-line camera. *Remote Sens.* **2022**, *14*, 1157. [CrossRef]
40. Liu, D. Study on Formation Mechanism-Prediction Analysis of Geologic Hazards in Fushun Coalfield. Ph.D. Thesis, Northeastern University, Shenyang, China, 2009.
41. Johnson, E.A. Geology of the Fushun Coalfield, Liaoning Province, People's Republic of China. *Int. J. Coal Geol.* **1990**, *14*, 217–236. [CrossRef]
42. Li, Z.C. Study on Deformation Mechanism and Failure Prediction of Landslide in West Open-Pit Mine in Fushun. Ph.D. Thesis, Jilin University, Changchun, China, 2017.
43. Liu, B.; Sun, X.; Di, K.; Liu, Z. Accuracy analysis and validation of ZY-3's sensor corrected products. *Remote Sens. Nat. Resour.* **2012**, *95*, 36–40.
44. Zhang, G. Rectification for High Resolution Remote Sensing Image under Lack of Ground Control Points. Ph.D. Thesis, Wuhan University, Wuhan, China, 2005.
45. Dai, W.; Chen, K.; Wang, C.; Li, M.; Tao, Y. Topographic change detection thatconsiders the spatial autocorrelation of DEM errors. *J. Geo-Inf. Sci.* **2022**, *24*, 2297–2308.
46. Ma, J.; Jiang, X.; Fan, A.; Jiang, J.; Yan, J. Image matching from handcrafted to deep features: A survey. *Int. J. Comput. Vis.* **2021**, *129*, 23–79.
47. Lowe, D.G. Distinctive image features from scale-invariant keypoints. *Int. J. Comput. Vis.* **2004**, *60*, 91–110. [CrossRef]
48. Von Gioi, R.G.; Jakubowicz, J.; Morel, J.M.; Randall, G. LSD: A fast line segment detector with a false detection control. *IEEE Trans. Pattern Anal. Mach. Intell.* **2010**, *32*, 722–732. [CrossRef] [PubMed]
49. Zhang, L.L.; Koch, R. An efficient and robust line segment matching approach based on LBD descriptor and pairwise geometric consistency. *J. Vis. Commun. Image Represent.* **2013**, *24*, 794–805. [CrossRef]
50. Jiang, Y.H.; Zhang, G.; Tang, X.M.; Zhu, X.Y.; Qin, Q.Q.; Li, D.R.; Fu, X.K. High accuracy geometric calibration of ZY-3 three-line image. *Acta Geod. Cartogr. Sin.* **2013**, *42*, 523–529+553.
51. Pan, H.; Tao, C.; Zou, Z. Precise georeferencing using the rigorous sensor model and rational function model for ZiYuan-3 strip scenes with minimum control. *ISPRS-J. Photogramm. Remote Sens.* **2016**, *119*, 259–266. [CrossRef]

Disclaimer/Publisher's Note: The statements, opinions and data contained in all publications are solely those of the individual author(s) and contributor(s) and not of MDPI and/or the editor(s). MDPI and/or the editor(s) disclaim responsibility for any injury to people or property resulting from any ideas, methods, instructions or products referred to in the content.